PVP-Modified Multifunctional Bi₂WO₆ Nanosheets for Enhanced CT Imaging and Cancer Radiotherapy

Yifan Hao,[⊥] Bo Peng,[⊥] Chao Si, Bo Wang, Chengfeng Luo, Menghao Chen, Cheng Luo, Baijuan Gong,* and Zhimin Li*

ACCESS | Metrics & More | Article Recommendations | Supporting Information

ABSTRACT: Malignant tumors are one of the main causes of human death. The clinical treatment of malignant tumors is usually surgery, chemotherapy, radiotherapy, and so forth. Radiotherapy, as a traditional and effective treatment method for cancer, is widely used in clinical practice, but the radiation resistance of tumor cells and the toxic side effects to normal cells are still the Achilles heel of radiotherapy. Multifunctional inorganic high-atom nanomaterials are expected to enhance the effect of tumor radiotherapy. Tungsten and bismuth, which contain elements with high atomic coefficients, have strong X-ray energy attenuation capability. We synthesized Bi₂WO₆ nanosheets (NSs) using a hydrothermal synthesis method and modified polyvinylpyrrolidone (PVP) on their surface to make them more stable. PVP−Bi₂WO₆ NSs have a variety of effects after

absorbing X-rays (such as the photoelectric effect and Compton effect) and release a variety of particles such as photoelectrons, Compton electrons, auger electrons, and so forth, which can react with organic molecules or water in cells, generate a large number of free radicals, and promote cell apoptosis, thereby improving the effect of radiotherapy. We show through γ-H2AX and DCFH-DA probe analysis experiments that PVP−Bi₂WO₆ NSs can effectively increase cell DNA damage and reactive oxygen species formation under X-ray irradiation. Clone formation analysis showed that PVP−Bi₂WO₆ NSs can effectively suppress cell colony formation under X-ray irradiation. These versatile functions endow PVP−Bi₂WO₆ NSs with enhanced radiotherapy efficacy in animal models. In addition, PVP−Bi₂WO₆ NSs can also be used as contrast agents for X-ray computed tomography (CT) imaging with obvious effects. Therefore, PVP−Bi₂WO₆ NSs can be used as CT imaging contrast agents and tumor radiotherapy sensitizers and have potential medical applications.
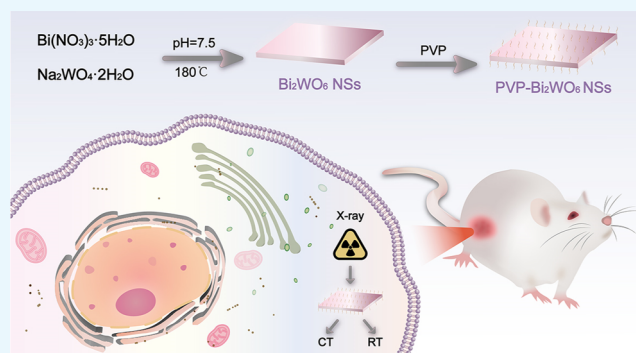
INTRODUCTION

Oral squamous cell carcinoma is the most common malignant tumor in the oral and maxillofacial region. Its incidence is gradually increasing,[1,2] and it is considered to be the main cause of death from oral diseases in many countries.[3] Moreover, the global cancer diagnosis rate and mortality rate have been on the rise in the past decade.[4] At present, clinical treatment methods for malignant tumors often include surgery, chemotherapy, radiotherapy, and so forth. Radiotherapy, as a traditional and effective treatment method for cancer, is widely used in clinical practice. Radiotherapy is often used in conjunction with other treatment methods to treat tumors.[5,6] Radiotherapy is the use of high-energy ionizing radiation such as X-rays and γ-rays as well as particle radiation, including particles such as α particles or β particles, electrons, protons, or neutron beams for tumor ablation.[7,8] The basic principle of radiotherapy is that ionizing radiation reacts with substances in tumor cells during radiotherapy. Ionizing radiation can directly or indirectly react with biological molecules (such as proteins, lipids, and so forth) in the tissue, and DNA is the main target

molecule.[4] On the one hand, it can directly ionize DNA molecules, causing DNA single-strand or double-strand breaks and base cross-linking and other types of damage, leading to the termination of cell division and cell proliferation; on the other hand, high-energy rays indirectly react with water in the tissue to generate reactive oxygen species (ROS) such as ●OH, ●H, H_2O^+, and $●O^{2−}$. ROS can damage biomolecules through chemical reactions; especially, ●OH can bind to DNA, cause DNA to undergo electron transfer and be oxidized, and induce cell DNA damage, leading to cell damage or apoptosis.[9−12] However, in the process of clinical treatment, the indirect damage of ionizing radiation to normal tissues, the hypoxic environment inside tumor cells, and the radiation resistance of
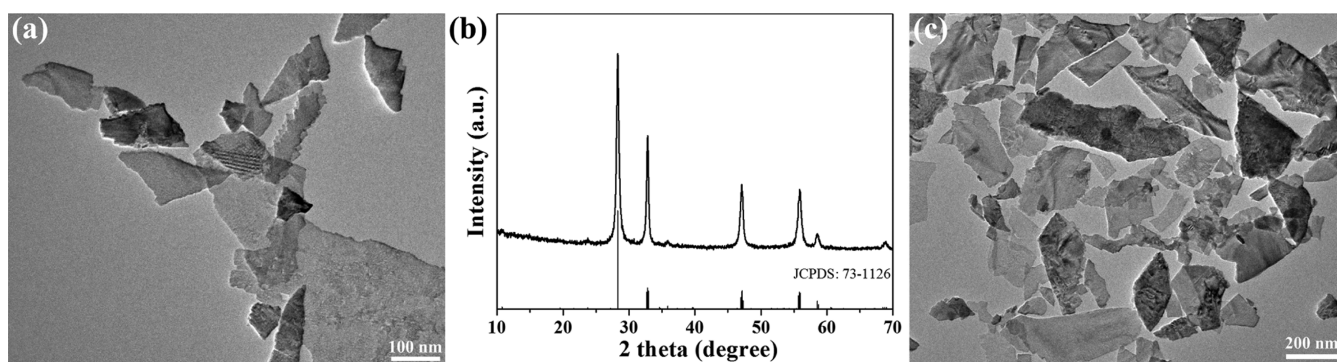
Figure 1. (a) TEM image of Bi_2WO_6 NSs. (b) Powder XRD patterns of Bi_2WO_6 NSs. (c) TEM image of PVP−Bi_2WO_6 NSs.

tumor cells have limited the further development of radiotherapy in the clinic to a certain extent. Moreover, in a low-oxygen environment, DNA double-strand damage can be repaired.[13] Therefore, studying how to reduce the radiation resistance of tumor cells, improve the radiation sensitivity of tumor cells, and improve the tumor microenvironment has certain clinical value.[11,14,15]

The emergence of radiotherapy sensitizers may be expected to solve this problem, which can increase the deposition of radiation in the tumor site, improve the hypoxia in the tumor site, and enhance the production of ROS in tumor cells.[16−18] In recent years, studies have found that nanoparticles containing a high atomic number can be expected to be used as radiotherapy sensitizers to enhance the radiosensitivity of tumor cells, thereby improving the effect of radiotherapy and reducing normal tissue damage.[19−22] Similar to heterogeneous photocatalysis, the mechanism of radiocatalysis is also under the irradiation of high-energy rays through a series of reactions to generate highly active singlet oxygen, thereby damaging DNA.[23] Nanoparticles with a high atomic number have a variety of effects (such as the photoelectric effect and Compton effect) after absorbing rays and release a variety of particles such as photoelectrons, Compton electrons, and auger electrons that react with organic molecules or water in cancer cells to generate a large number of free radicals, which can improve the effect of radiotherapy and have potential medical applications.[24] Compton scattering is an inelastic scattering of photons by electrons, and it is one of the most important interactions in radiotherapy. After colliding with the electrons, the energy of the incident photons is reduced, so the radiation dose can be deposited at a local location. The photoelectric effect is that the electrons in the atomic shell absorb the energy of incident rays and are emitted to ionize surrounding biomolecules. High-Z nanomaterials can be enabled to increase the ionizing radiation dose at the tumor site.[25] With the development of nanomedicine, multifunctional inorganic high atomic coefficient nanomaterials have attracted widespread attention and have clinical significance in enhancing the effect of cancer radiotherapy.[26,27] W ($Z = 74$) and Bi ($Z = 83$) containing high atomic coefficient elements have strong X-ray energy attenuation ability. Hossain and Su controlled the concentration of nanoparticles to 350 mg·g^{-1} under a 50 kVp radiation source, and the radiosensitization effect of nanobismuth was 1.25 times and 1.29 times stronger than that of nano-gold and nano-platinum, respectively. It is concluded that bismuth nanoparticles have a stronger sensitizing effect than gold and platinum nanoparticles at the same nanometer size, particle concentration, and action site.[28] At 100 keV, the X-ray

mass attenuation coefficients of Bi and W elements are 5.74 and 4.44 cm^2/g, respectively.[29,30] By modifying the surface of nanoparticles in different ways, nanoparticles can also be used for active targeting or therapy, and multimodal imaging, which is expected to be used as a contrast agent for X-ray computed tomography (CT) imaging. CT is one of the most widely used imaging methods in clinical practice, which has the advantages of high efficiency, short scanning time, and high resolution. Ordinary CT is suitable for different tissues with large density differences, but it is difficult for the density differences between soft tissues to form a clear contrast on the image. Therefore, the application of contrast agents can selectively enhance the image contrast between the target soft tissue and surrounding tissues and improve CT sensitivity.[31] Iodide is the earliest and most widely used CT contrast agent in clinical practice, but the imaging time of this contrast agent is short, and its high osmotic pressure, high viscosity, and electric charge often trigger contrast agent reactions, posing a threat to the life safety of patients.[32] Compared with traditional small-molecule contrast agents, nanoparticles can load a large number of contrast elements; have long blood circulation half-life, low renal clearance, and capillary leakage; and can accumulate in the tumor site through the enhanced permeation and retention effect.[33] In recent years, Bi_2WO_6 nanosheets (NSs) have been studied as a powerful multifunctional platform with the ability of photothermal therapy and photodynamic therapy.[34] Bi_2WO_6 NSs can kill tumor cells and achieve local photothermal ablation of tumors under the irradiation of ultraviolet to near-infrared lasers. At the same time, ●OH free radicals are generated without consuming oxygen molecules, so that these Bi_2WO_6 NSs can play a photodynamic killing effect in an oxygen-free manner during cancer treatment.[35] In addition, Bi_2WO_6 NSs have a variety of effects after absorbing X-rays (such as the photoelectric effect and Compton effect) and release a variety of particles such as photoelectrons, Compton electrons, and auger electrons, which have the potential to be used in tumor radiotherapy.[36]

Therefore, we studied the radiosensitization effect of Bi_2WO_6 NSs in tumor radiotherapy. In this study, we use a reasonable design to increase the amount of nanomaterials in tumors, enhance the sensitivity of nanomaterials under X-ray, and enhance their ability to produce singlet oxygen and better kill tumor cells. Therefore, we prepared Bi_2WO_6 NSs. In addition, the surface of the NSs was modified with PVP, which is stable and negatively charged. In the blood circulation, it can effectively avoid being marked and removed by the same negatively charged labeling factors. Therefore, PVP−Bi_2WO_6 NSs were beneficial to the accumulation in tumors, and the
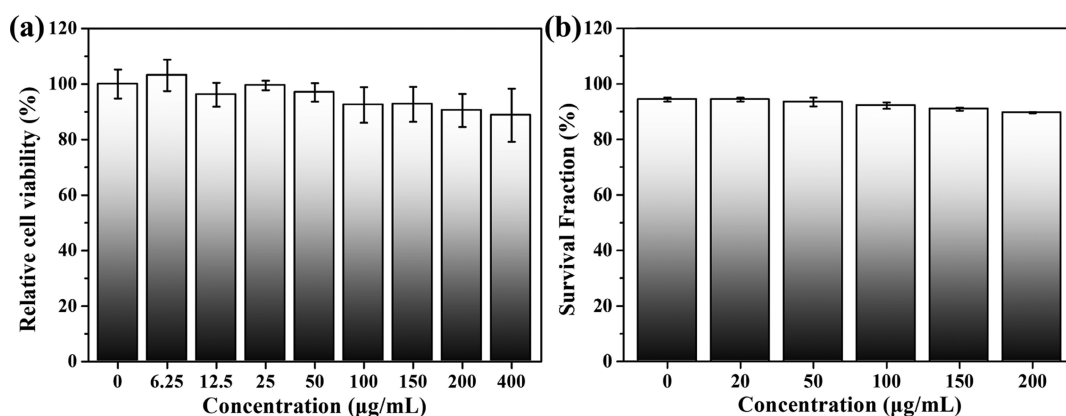
Figure 2. (a) In vitro cytotoxicity of PVP−Bi$_2$WO$_6$ NSs with different concentrations was tested by CCK-8. (b) In vitro cytotoxicity of PVP−Bi$_2$WO$_6$ NSs with different concentrations was tested by flow cytometry.
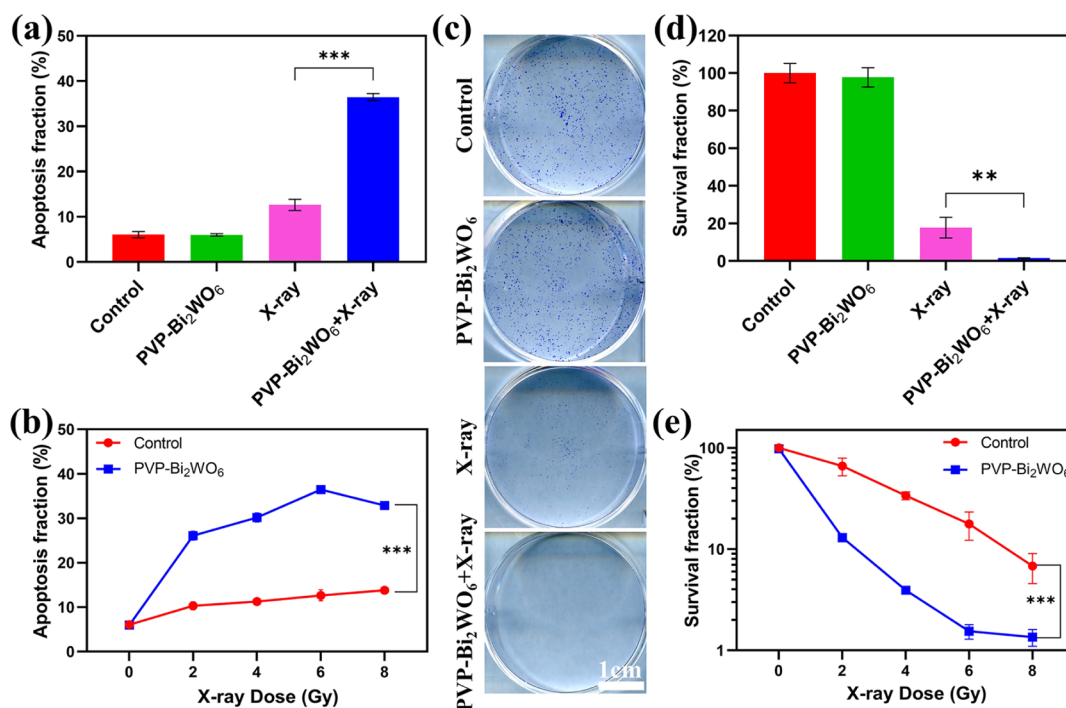

Figure 3. (a) The apoptosis of CAL27 cells under different treatments was conducted by flow cytometry analysis. (b) The apoptosis of CAL27 cells under different treatments and X-ray dose was conducted by flow cytometry analysis. (c) Clonogenic assay of CAL27 cells under different treatments (X-ray dose: 6 Gy). (d) Survival fraction of CAL27 cells under different treatments (X-ray dose: 6 Gy). (e) Survival fraction of CAL27 cells under different treatments and X-ray doses. **$P < 0.01$ and ***$P < 0.001$.

accumulation rate showed a trend of increasing first and then decreasing gradually, reaching the highest at about 24 h. PVP−Bi$_2$WO$_6$ NSs contain both tungsten and bismuth nanomaterials that are radiosensitizing elements, and the sheet structure has a large specific surface area. These factors greatly enhance the radiosensitization capabilities of nanomaterials. Moreover, because of the presence of two metal elements, tungsten and bismuth, PVP−Bi$_2$WO$_6$ NSs can also be used as CT imaging contrast agents to locate tumors. The lamellar structure has a large specific surface area, which can increase the ray absorption cross section, deposit high-energy ray energy, promote the generation of free radicals, and enhance DNA damage, which greatly improves the radiosensitization ability of nanomaterials. In addition, due to the high atomic numbers of the two metal elements, tungsten and bismuth, PVP−Bi$_2$WO$_6$ NSs can also be used as CT imaging contrast agents to

show good CT imaging capabilities. In vitro anti-tumor results show that PVP−Bi$_2$WO$_6$ NSs have the function of enhancing the destruction of cancer cells under radiation irradiation. The in vivo anti-tumor results also clearly show that the presence of PVP−Bi$_2$WO$_6$ NSs after radiation exposure can effectively reduce solid tumor tissue. We believe that after continuous exploration and research, PVP−Bi$_2$WO$_6$ NSs will definitely play an active role in future clinical treatments.

■ RESULTS AND DISCUSSION

We synthesized Bi$_2$WO$_6$ NSs by a simple hydrothermal method, and the morphology is shown in Figure 1a, which is a two-dimensional lamellar structure. The X-ray diffraction (XRD) spectrum showed their good crystallinity, and it can be well matched with orthorhombic Bi$_2$WO$_6$ (JCPDS: 73-1126, Figure 1b). Then, we modified PVP on their surface to prepare
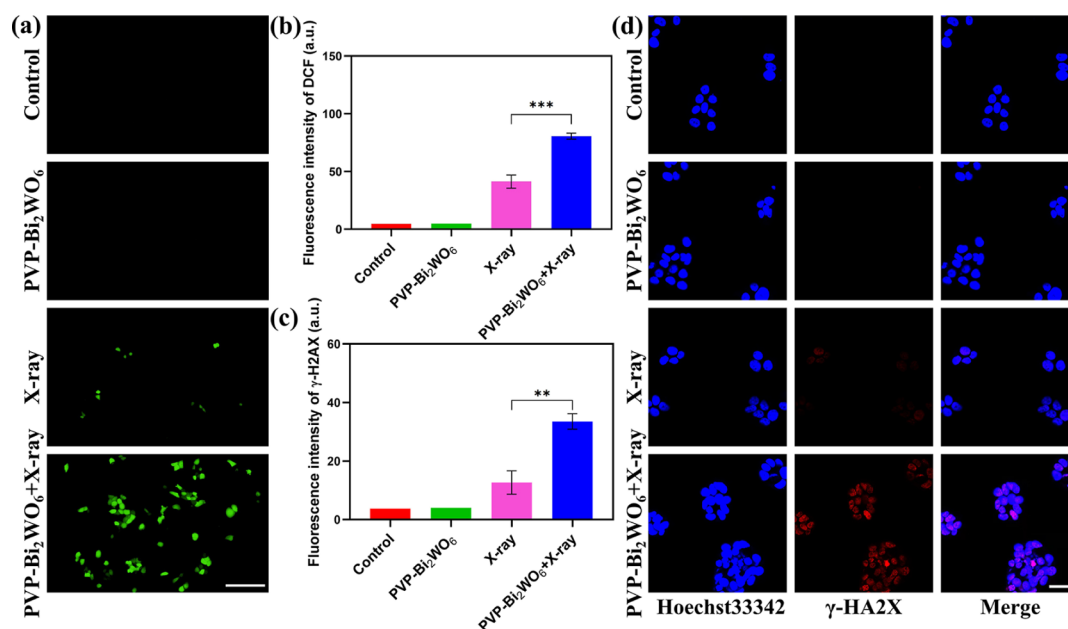
Figure 4. (a) ROS detection in CAL27 cells under different treatments by using DCFH-DA as the probe (scale bar is 100 μm). (b) Average signal intensity of DCFH-DA after different treatments. (c) Average signal intensity of γ-H2AX after different treatments. (d) γ-H2AX staining in CAL27 cells under different treatments (scale bar is 50 μm). **$P < 0.01$ and ***$P < 0.001$.

PVP−Bi_2WO_6 NSs. The TEM image showed that the obtained PVP−Bi_2WO_6 NSs basically maintained the same morphology as Bi_2WO_6 NSs (Figure 1c). PVP modification greatly improved the water-solubility of Bi_2WO_6 NSs. On the one hand, PVP is negatively charged and can maintain the colloidal stability through electrostatic repulsion. On the other hand, space-occupying PVP ligands can stabilize Bi_2WO_6 NSs through spatial effects.[37] The enhanced water-solubility could enhance the stability of NSs. PVP can also reduce the toxicity of nanoparticles. Many studies have shown that PVP is a kind of ligand with very low toxicity and has certain advantages in improving biocompatibility.[38,39]

We tested and analyzed the in vitro cytotoxicity of PVP−Bi_2WO_6 NSs through CCK-8. As shown in Figure 2a, CAL27 cell viability is still above 90% at concentrations of 100 and 200 μg/mL. At the highest concentration (400 μg/mL), the cytotoxicity is still low, and the cell vitality is still above 85%. This further proves that PVP−Bi_2WO_6 NSs have lower cytotoxicity and also means that PVP−Bi_2WO_6 NSs have good biocompatibility in biomedical applications. In addition, we used flow cytometry to detect the effect of PVP−Bi_2WO_6 NSs on the apoptosis of CAL27 cells. The results are shown in Figure 2b. There is no significant difference in the apoptosis rate of cells compared with the control group at different concentrations, even though at a higher concentration (200 μg/mL), the effect of PVP−Bi_2WO_6 NSs on cell apoptosis is still very small and can be ignored.

We analyzed the apoptosis rate of cells under different irradiation doses using flow cytometry. As shown in Figure 3a, compared with the control group, there was no significant difference in the apoptosis rate of the PVP−Bi_2WO_6 group, and the apoptosis rate of the simple X-ray irradiation group increased; compared with the simple irradiation group, the proportion of live cells in the PVP−Bi_2WO_6 + X-ray irradiation group is less, and the apoptotic rate is higher (Figure S1). Whether it is a low dose or a high dose, the cell apoptosis rate after co-culturing with the PVP−Bi_2WO_6 NSs is higher than

that of the irradiation alone group (Figure 3b). We did a clone formation test to evaluate the radiosensitization effect of PVP−Bi_2WO_6 NSs. As shown in Figure 3c, the combination of PVP−Bi_2WO_6 NSs and X-ray can inhibit the clone formation to a great extent. After co-culturing with PVP−Bi_2WO_6 NSs alone, the survival rate of CAL27 cells was 97.7%. When only X-ray irradiation (6 Gy) was applied, the survival rate of CAL27 cells decreased to 17.7%. However, after co-cultivation with PVP−Bi_2WO_6 and X-ray irradiation, the survival rate of the cells dropped to 1.5%, which was significantly lower than that in the X-ray irradiation group (Figure 3d). Under different irradiation doses (2, 4, 6, and 8 Gy), the colony formation rate of the cell group co-cultured with PVP−Bi_2WO_6 NSs was significantly lower than that of the control group (Figure 3e).

In addition, ROS probe DCFH-DA can combine with ROS to emit green fluorescence, and the relative strength of fluorescence can reflect the relative content of ROS in cells. The intensity of green fluorescence in the control group and PVP−Bi_2WO_6 NS group was extremely low, which proved that ROS generation was very low, and simple co-culture with PVP−Bi_2WO_6 NSs could not improve the ROS content in CAL27 cells. X-ray irradiation can produce a small amount of ROS in cells, but the content is relatively low. Under X-ray, PVP−Bi_2WO_6 NSs can generate a large number of ROS, which helps to promote cell apoptosis (Figure 4a). In addition to direct comparison of fluorescence photographs, the fluorescence intensity was also quantitatively analyzed. The results showed that the fluorescence intensity of the PVP−Bi_2WO_6 NSs + X-ray group was significantly higher than that of other groups, which proves that PVP−Bi_2WO_6 NSs can effectively increase the level of ROS in CAL27 cells under X-ray irradiation (Figure 4b).

Finally, immunofluorescence staining was used to measure DNA damage in cells. Damaged DNA can be recognized by γ-H2AX and labeled with red fluorescence. Both PVP−Bi_2WO_6 NSs and X-ray alone have a low effect on DNA damage. However, under X-ray irradiation, PVP−Bi_2WO_6 NSs can
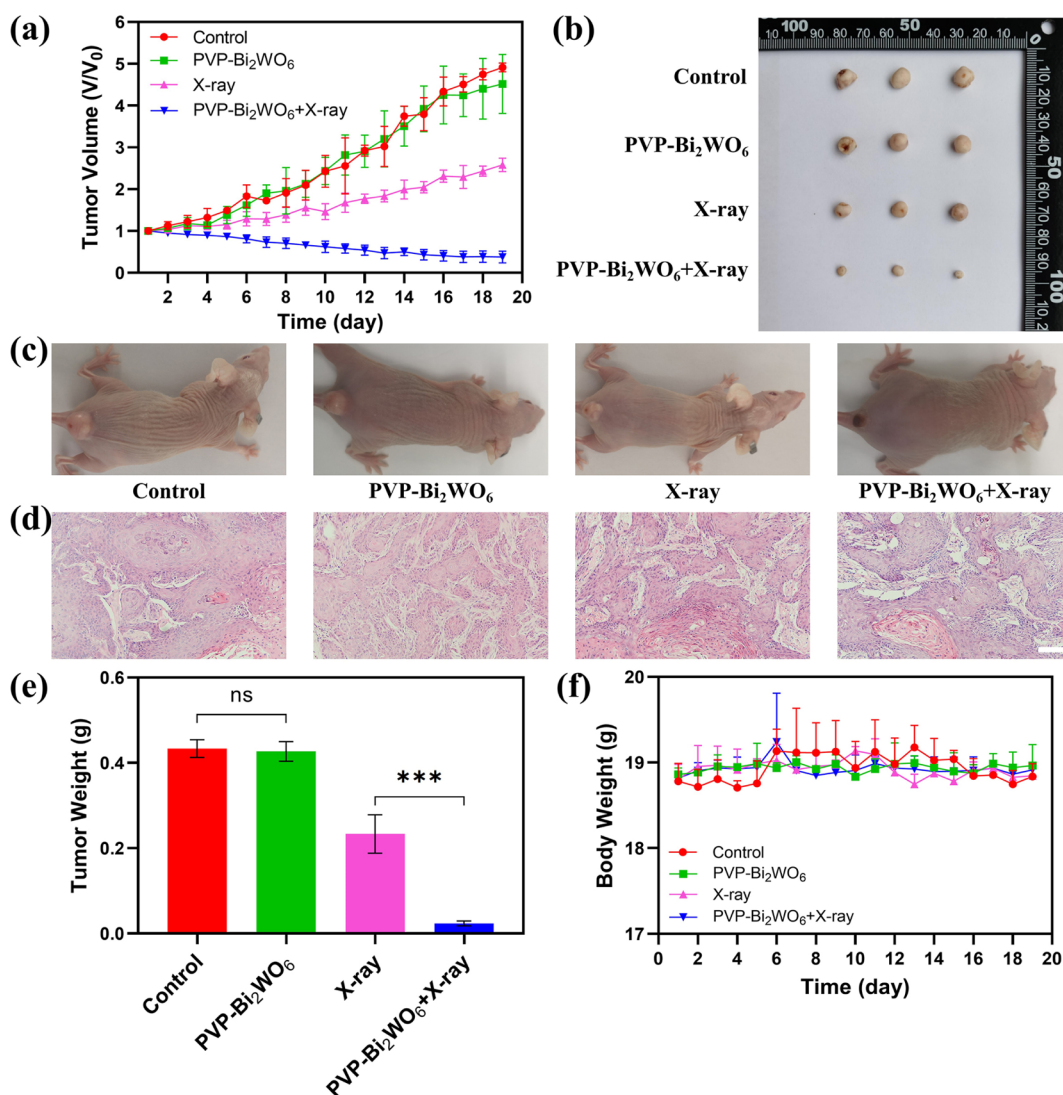
Figure 5. In vivo synergistic therapy. The mice are divided into four groups: control group, PVP−Bi$_2$WO$_6$ group, X-ray irradiation group, and PVP−Bi$_2$WO$_6$ + X-ray irradiation group. (a) Tumor volume of mice during 18 days. (b) Photographs of tumors at the end of treatment. (c) Photographs of typical mice at the end of treatment. The average tumor volume is 311, 292, 162, and 24 mm^3 for each group. (d) H&E staining of tumors at the end of treatment. The scale bar is 100 μm. (e) Average weights of tumors at the end of treatment. (f) Body weight curves of mice during 18 days. ns $P > 0.05$ (no significant difference) and ***$P < 0.001$.

cause large areas of DNA damage (Figure 4d). Quantitative analysis of fluorescence intensity showed that the fluorescence intensity of the PVP−Bi$_2$WO$_6$ NSs + X-ray group was 2.65 times that of the X-ray group, and the effect was very obvious (Figure 4c). These experiments indicate that PVP−Bi$_2$WO$_6$ NSs are expected to be used as radiotherapy sensitizers to enhance the radiotherapy effect on tumors.

In view of the remarkable results of the cell experiment, we further studied the radiotherapy effect of PVP−Bi$_2$WO$_6$ NSs in animals. After subcutaneously inoculating mice with CAL27 cells to establish the tumor models, the mice were randomly divided into four groups: (I) control group, (II) PVP−Bi$_2$WO$_6$ group, (III) X-ray irradiation group, and (IV) PVP−Bi$_2$WO$_6$ + X-ray irradiation group. In the exploration of the optimal time to apply radiation, the experimental results showed that the accumulation rate of PVP−Bi$_2$WO$_6$ NSs in CAL27 tumors showed a trend of gradually increasing at first and then gradually decreasing, and it reached the highest value at 24 h, which was 6.19% (Figure S2). Therefore, 24 h was identified as

the point in time to apply X-ray in animal experiments. In subsequent experiments, the tumor volume and the weight of the mice were measured every day. On the 18th day, the tumor volume and weight data could be used to intuitively compare the treatment effects. As shown in Figure 5a−c, the tumor volumes of the mice in the control group and in the PVP−Bi$_2$WO$_6$ group continued to increase. By the end of the treatment, the tumors had grown to about 300 mm^3. The fluctuation in the mice's weight suggested that the body's metabolism is out of whack, and the tumors are not well treated (Figure 5f). Compared with these two groups, the tumor volumes of the mice in the simple X-ray group were suppressed to a certain extent, and the tumor volumes were reduced. However, the tumor volumes of mice in the PVP−Bi$_2$WO$_6$ + X-ray group were significantly reduced, and the growth rate of the tumors was significantly inhibited (Figure 5a−c). At the same time, the fluctuation of body weight was small, and the mice were basically in a normal growth state, indicating that the tumors were highly treated and the growth
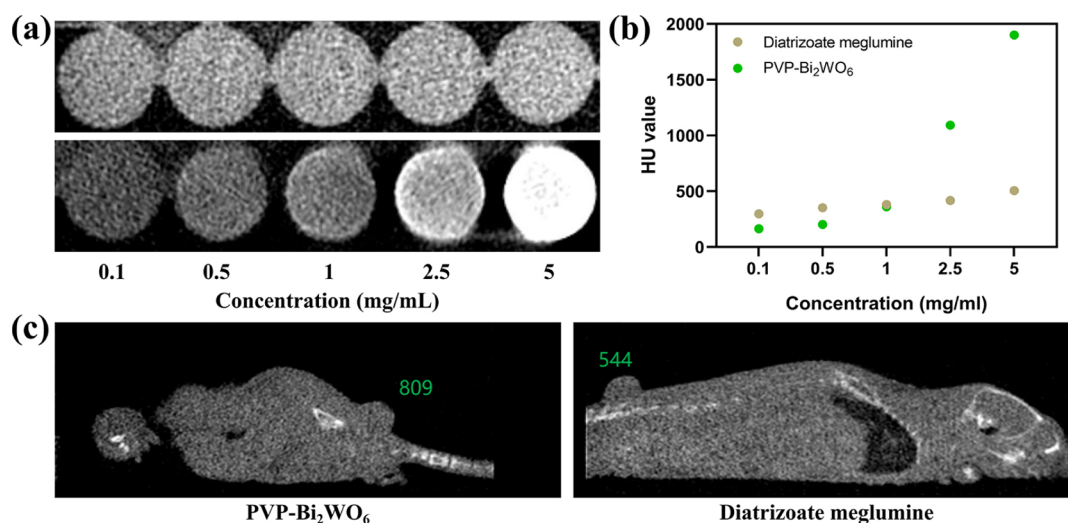
Figure 6. (a) CT images of diatrizoate meglumine and PVP−Bi$_2$WO$_6$ NSs. (b) HU value of diatrizoate meglumine and PVP−Bi$_2$WO$_6$ NSs in CT imaging at different concentrations. (c) HU value in CT imaging 24 h after injection of diatrizoate meglumine and PVP−Bi$_2$WO$_6$ NSs into the tail vein of mice, respectively.

of mice was not affected. Besides, this not only proved the low toxicity of nanomaterials, but it also proved the effective protection to the mouse during irradiation (Figure 5f). In Figure 5d,e, tumor weights and H&E-stained tumor sections also confirm the antitumor effects of PVP−Bi$_2$WO$_6$ NSs in vivo. Finally, we performed H&E staining on major organs (including heart, spleen, lung, liver, kidney, and testis) and observed the pathological manifestations of the tissues under an optical microscope. We observed that no obvious pathological manifestations were observed in the tissues of the four groups of mice (Figure S3). At the same time, we performed liver and kidney function analysis on the blood of each group of mice (Figures S4−S6). Compared with the control group, each treatment group showed no obvious toxicity. The above results all proved the good compatibility of PVP−Bi$_2$WO$_6$ NSs in vivo and low biological toxicity.

The results of in vitro CT imaging experiments showed that the CT imaging ability of PVP−Bi$_2$WO$_6$ NSs and meglumine is similar at a low concentration, but at a high concentration, the CT imaging ability of PVP−Bi$_2$WO$_6$ NSs is stronger (Figure 6a,b). In order to further prove the CT imaging ability of PVP−Bi$_2$WO$_6$ in mice, we injected PVP−Bi$_2$WO$_6$ NSs and diatrizoate meglumine into the mice via tail vein, respectively, and then compared their imaging effects. As shown in Figure 6c, the HU value of the tumor site in the control group is 544, and the HU value of the tumor site in the PVP−Bi$_2$WO$_6$ group is as high as 809, which further proves that PVP−Bi$_2$WO$_6$ NSs can reach the tumor site through the EPR effect and obtain better therapeutic effects.

CONCLUSIONS

We successfully prepared PVP-modified Bi$_2$WO$_6$ NSs by hydrothermal synthesis. The sheet-like structure gives it a large surface area and makes it have a strong absorption effect on X-ray. We have proved its good effect of inhibiting cell proliferation through the clone formation experiment, and the ROS experiment proved that it has a better effect of increasing the level of intracellular ROS. The γ-H2AX experiment further proved that PVP−Bi$_2$WO$_6$ NSs can significantly increase the level of DNA fragmentation under X-ray irradiation. In vivo experiments have further proved its powerful radiosensitization

effect. Through H&E staining of organs and liver and kidney function tests, we have not observed its toxicity to organs and tissues. The above experiments have effectively proved that PVP−Bi$_2$WO$_6$ NSs can be expected to be used as a radiotherapy sensitizers, thereby improving the therapeutic effect of radiotherapy and reducing its side effects, which has potential medical application value.

EXPERIMENTAL SECTION

Materials. Bi(NO$_3$)$_3$·5H$_2$O (99.0%) and Na$_2$WO$_4$·2H$_2$O (99.5%) were purchased from Aladdin. HNO$_3$ (AR) and KOH (AR) were purchased from Sinopharm Chemical Reagent Company. Poly(vinylpyrrolidone) (PVP, $M_w \sim 1\,300\,000$) was purchased from Sigma-Aldrich. Cell counting kit-8 (CCK-8), immunostaining permeabilization solution with Triton X-100, ROS assay kit, immunol staining fix solution, blocking buffer for immunol staining, immunol staining wash buffer, crystal violet staining solution, and Hoechst 33342 were all purchased from Beyotime. An annexin V-FITC/PI apoptosis detection kit was purchased from Solarbio. γ-H2AX (phosthoS139) antibody [EP854(2)Y] (AlexaFluor568) (ab206901) was purchased from Abcam.

Synthesis and Modification of PVP−Bi$_2$WO$_6$ NSs. First, 10 mmol Bi(NO$_3$)$_3$·5H$_2$O was dissolved in 4.5 mL of 20% HNO$_3$ aqueous solution under ultrasound, and then it was slowly added dropwise into the Na$_2$WO$_4$·2H$_2$O aqueous solution (5 mmol Na$_2$WO$_4$·2H$_2$O dissolved in 40 mL of deionized water). Next, the mixture was stirred for 1 h. After adjusting the pH to 7.5 by KOH, the mixture was transferred to a Teflon-lined autoclave and treated at 180 °C for 2 h. After cooling to room temperature, the mixture was centrifuged at 6000 rpm for 5 min, and then the precipitate was re-dispersed in water. This step needs to be repeated twice.[36]

In order to modify PVP, the PVP aqueous solution (30 mg of PVP dissolved in 5 mL of deionized water) was slowly added dropwise into the Bi$_2$WO$_6$ aqueous solution (30 mg of Bi$_2$WO$_6$ dissolved in 5 mL of deionized water). After sonicating for 2 h, the mixture was centrifuged at 6000 rpm for 5 min, and then the precipitate was re-dispersed in water. This step needs to be repeated twice. The final sample PVP−Bi$_2$WO$_6$ NSs were dispersed in deionized water.

Cell Experiments In Vitro. CAL-27 cells were selected for the study. CAL-27 cells, also named Centre Antoine Lacassagne-27 cells, were developed by J. Gioanni in 1982, derived from a lesion in the middle of the tongue of a 56-year-old white male. For the in vitro cytotoxicity assay, 100 μL of CAL27 cell suspension (5000 cells/well) was placed in a 96-well plate, and the culture plate was placed in an incubator for 24 h (37 °C, 5% CO$_2$). Then,10 μL of PVP–Bi$_2$WO$_6$ at different concentrations was added to each well (0, 6.25, 12.5, 25, 50, 100, 150, 200, and 400 μg/mL). The 96-well plate was placed in an incubator and was allowed to continue to incubate for 24 h. Then, the original medium was discarded, and the cells were washed twice with phosphate buffered saline (PBS). 10 μL of CCK8 solution was added to each well. The culture plate was incubated in an incubator for 2 h. The absorbance at 450 nm was measured with a microplate reader. In the cell apoptosis assay, 100,000 CAL27 cells were added to each well of a six-well plate, and they were placed in an incubator for 24 h. Different concentrations of PVP–Bi$_2$WO$_6$ (0, 20, 50, 100, 150, and 200 μg/mL) were added to the wells and incubated with the cells overnight. The original culture medium was collected, the cells were washed 3 times with PBS, and then the cells were resuspended in a binding buffer. A annexin V-FITC/PI apoptosis detection kit was used for flow cytometric analysis of apoptosis. In the clonogenic assay, 1,500 of CAL27 cells were added to each well of a six-well plate, the culture plate was placed in an incubator for 24 h (37 °C, 5% CO$_2$), and then, 20 μL of PVP–Bi$_2$WO$_6$ (concentration of 100 μg/mL) was added to each well. After culturing for 24 h, each orifice plate was irradiated with different doses (0, 2, 4, 6, and 8 Gy) of X-ray, and they were put in an incubator to continue culturing. The medium was changed every 2–3 days, and the formation of cell colonies was observed frequently until the formation of visible colonies (50–100). The original medium was discarded in the well plate, the cells were washed with PBS 3 times, the cells were fixed with 4% paraformaldehyde at room temperature for 15 min, stained with crystal violet staining solution for 10 min, and the six-well plate was washed with distilled water. Under the microscope, the number of cells proliferating more than 50 was counted, the number of each well was recorded, and photographs were taken of the six-well plate. The average survival score was obtained from three parallel samples. In the apoptosis assay, CAL27 cells (50,000 cells per well) were added to a six-well plate and placed in an incubator for 24 h. After the cells were completely attached, PVP–Bi$_2$WO$_6$ (100 μg/mL) was added to the wells to co-culture these cells overnight. Then, they were irradiated with X-rays, culturing was continued for 24 h, the original culture fluid was collected, the cells and centrifuge were digested, the cells were washed with PBS 3 times, and the cells were resuspended with the binding buffer. An annexin V-FITC/PI apoptosis detection kit was used for flow cytometric analysis of apoptosis. In the ROS experiment in vitro, CAL27 cells were added to a six-well plate (50,000 cells per well), 20 μL of PVP–Bi$_2$WO$_6$ (100 μg/mL) was added after culturing overnight, and co-culturing was continued for 4 h. The cells were washed 3 times with PBS. Serum-free medium was used to dilute the DCFH-DA probe by a thousand times; then, the diluted probe was added to the well and incubated for 20 min, and the cells were carefully washed with serum-free medium 3 times. Finally, 1.5 mL of serum-free culture medium was added to each well. The cells were irradiated with X-ray (6 Gy) and then detected using a fluorescence microscope (excitation

wavelength: 488 nm, emission wavelength: 525 nm). In the DNA double-stranded breaks assay, CAL27 cells were cultured in a confocal dish with a density of 50,000 cells per dish and cultured in an incubator for 24 h (37 °C, 5% CO$_2$). Then, the cells were divided into four groups: (1) control group, (2) PVP–Bi$_2$WO$_6$ group, (3) X-ray irradiation group, and (4) PVP–Bi$_2$WO$_6$ + X-ray irradiation group. Then, PVP–Bi$_2$WO$_6$ (100 μg/mL) was added to the cells of groups (2) and (4). It was incubated with the cells for 24 h, and the cells in groups (3) and (4) were irradiated at 6 Gy (1 Gy/min) with X-ray. After culturing for 4 h, immunofluorescence staining of γ-H2AX was performed. The cells were fixed with immunostaining fixative for 10 min and then washed 3 times with immunostaining washing solution. Then, the cells were permeabilized with immunostaining permeate for 15 min, and the cells were washed 3 times. Then, the cells were blocked with immunostaining blocking solution for 2 h. The blocking solution was discarded, diluted γ-H2AX (diluted 1:1000 with the primary antibody dilution solution) was added, and the cells were incubated overnight at 4 °C in the dark. Next, excess antibodies were removed, the cells were washed with a washing solution 3 times, the nuclei were stained with Hoechst 33342 (diluted 1:100 with PBS), and then, a laser confocal microscope was used to detect the fluorescence intensity of each group. (Primary antibody excitation wavelength: 590 nm, emission wavelength: 617 nm; Hoechst33342 excitation wavelength: 346 nm, emission wavelength: 460 nm.)

CT Imaging Assay In Vitro. In the CT imaging assay in vitro, deionized water was used to configure PVP–Bi$_2$WO$_6$ NSs into solutions of different concentrations, with concentration gradients of 0.1, 0.5, 1, 2.5, and 5 mg/mL, respectively. A CT machine was used to test the effect of CT imaging. To more intuitively reflect the effect of CT imaging, the corresponding CT signal values of each sample were read in the reading system, and the signal intensity of each group was compared with a numerical value. (The voltage is 60 kV, the current is 1 mA, and the radiation dose is 0.1 mGy.)

Animal Experiments. Five-week-old BALB/c nude mice were selected, and the mice were purchased from Beijing Vital River Laboratory Animal Technology Co., Ltd. All the animal procedures were performed in accordance with the Guidelines for the Care and Use of Laboratory Animals of Jilin University and approved by the Animal Ethics Committee of College of Basic Medical Sciences, Jilin University. After being adaptively raised in a barrier environment for 1 week, a tumor-bearing mouse model was established. 1,200,000 of CAL27 cells were injected subcutaneously into the middle part of the back of the mouse. After that, the mice were raised normally, the tumor size of the mice was observed and measured, and the tumor volume was estimated according to the formula: $V = ab^2/2$ (where a and b are the length and width of the tumor, respectively). When the tumor volume reached 50–60 mm^3, the mice were randomly divided into four groups ($n = 3$): (I) control group, (II) PVP–Bi$_2$WO$_6$ group, (III) X-ray irradiation group, and (IV) PVP–Bi$_2$WO$_6$ + X-ray irradiation group. Then, mice in groups (I) and (III) were injected with 40 μL of normal saline through the tail vein, and tumor-bearing mice in groups (II) and (IV) were injected with 40 μL of PVP–Bi$_2$WO$_6$ (5 mg/mL) through the tail vein; (III) and (IV) X-ray irradiation was performed 24 h after the tail vein injection in the group, the irradiation dose was 6 Gy, 1 Gy/min. After irradiation, the mice were raised normally, and the body weight

and tumor size of the mice were measured and recorded every day to compare the treatment effects of each group. After 18 days of continuous measurement, the mice were sacrificed, and the tumors and major organs (including heart, spleen, lung, liver, kidney, and testis) of the mice were taken out, and these tissues were weighed and stained. The tumors and main organs of the mice were fixed with 4% paraformaldehyde, dehydrated, embedded in paraffin, and frozen sectioned. Finally, the histological section was co-stained with hematoxylin and eosin (H&E) and then imaged using an optical microscope to analyze and compare the pathological manifestations of each tissue. The blood of the mice was centrifuged to obtain the upper serum, and the serum was tested for liver and kidney function.

Characterization. XRD was measured using an Empyrean X-ray diffractometer with Cu K radiation (λ = 1.5418 Å). Transmission electron microscopy (TEM) was conducted using a JEM-2100F transmission electron microscope (200 kV). The absorbance of cells in the plate was detected using a Bio-tek microplate reader at a 490 nm wavelength. The apoptosis was measured using a BD Biosciences FACScan flow cytometer. The ROS fluorescence intensity was monitored using an Olympus U-LH100HG fluorescence microscope. The DNA double-stranded break staining was observed using C2 laser scanning confocal microscopy. The X-ray irradiation was treated with a PXi X-RAD 320 X-ray irradiator (1 Gy/min). The CT imaging capability was assessed with Planmeca Cone beam CT (60 kV, 1 mA). The HU value was measured using Invivo 5.0 software..

■ ASSOCIATED CONTENT

ⓈI Supporting Information

The Supporting Information is available free of charge at https://pubs.acs.org/doi/10.1021/acsomega.2c01591.

> Additional flow cytometry data, tumor accumulation rates, H&E-stained organ slices, blood liver function test data, blood renal function test data, and blood ion detection data (PDF)

■ AUTHOR INFORMATION

Corresponding Authors

Baijuan Gong − *Department of Orthodontics, School of Stomatology, China Medical University, Shenyang 110002, P. R. China*; Email: lzmxx@aliyun.com

Zhimin Li − *Department of Oral Radiology, School of Stomatology, China Medical University, Shenyang 110002, P. R. China*; ⓞ orcid.org/0000-0003-0892-4999; Email: zmli@cmu.edu.cn

Authors

Yifan Hao − *Department of Oral Radiology, Hospital of Stomatology and Jilin Provincial Key Laboratory of Tooth Development and Bone Remodeling, School and Hospital of Stomatology, Jilin University, Changchun 130021, P. R. China*

Bo Peng − *Department of Oral Radiology, School of Stomatology, China Medical University, Shenyang 110002, P. R. China*

Chao Si − *Department of Oral Radiology, Hospital of Stomatology and Jilin Provincial Key Laboratory of Tooth Development and Bone Remodeling, School and Hospital of Stomatology, Jilin University, Changchun 130021, P. R. China*

Bo Wang − *Department of Oral Radiology, School of Stomatology, China Medical University, Shenyang 110002, P. R. China*

Chengfeng Luo − *Department of Oral Radiology, School of Stomatology, China Medical University, Shenyang 110002, P. R. China*

Menghao Chen − *Department of Oral Radiology, School of Stomatology, China Medical University, Shenyang 110002, P. R. China*

Cheng Luo − *Department of Orthodontics, School of Stomatology, China Medical University, Shenyang 110002, P. R. China*

Complete contact information is available at:
https://pubs.acs.org/10.1021/acsomega.2c01591

Author Contributions

[⊥]Y.F.H. and B.P. contributed equally.

Author Contributions

Y.F.H. and B.P. contributed equally to this work. Z.M.L. and B.J.G. supervised and proposed the project. Y.F.H. and B.P. designed and performed the experiments and co-wrote the paper. C.S., B.W., C.F.L., M.H.C., and C.L. participated in most experiments. All authors have given approval to the final version of the manuscript.

Notes

The authors declare no competing financial interest.

■ ACKNOWLEDGMENTS

■ REFERENCES

(1) Ng, J. H.; Iyer, N. G.; Tan, M.-H.; Edgren, G. Changing epidemiology of oral squamous cell carcinoma of the tongue: A global study. *Head Neck* **2017**, *39*, 297−304.

(2) Du, M.; Nair, R.; Jamieson, L.; Liu, Z.; Bi, P. Incidence Trends of Lip, Oral Cavity, and Pharyngeal Cancers: Global Burden of Disease 1990-2017. *J. Dent. Res.* **2020**, *99*, 143−151.

(3) Almangush, A.; Mäkitie, A. A.; Triantafyllou, A.; de Bree, R.; Strojan, P.; Rinaldo, A.; Hernandez-Prera, J. C.; Suárez, C.; Kowalski, L. P.; Ferlito, A.; Leivo, I. Staging and grading of oral squamous cell carcinoma: An update. *Oral Oncol.* **2020**, *107*, 104799.

(4) Huang, R.-X.; Zhou, P. K. DNA damage response signaling pathways and targets for radiotherapy sensitization in cancer. *Signal Transduction Targeted Ther* **2020**, *5*, 60.

(5) Barton, M. B.; Jacob, S.; Shafiq, J.; Wong, K.; Thompson, S. R.; Hanna, T. P.; Delaney, G. P. Estimating the demand for radiotherapy from the evidence: A review of changes from 2003 to 2012. *Radiother. Oncol.* **2014**, *112*, 140−144.

(6) Wang, H.; Mu, X.; He, H.; Zhang, X.-D. Cancer Radiosensitizers. *Trends Pharmacol. Sci.* **2018**, *39*, 24−48.

(7) Wang, X.; Guo, Z.; Zhang, C. Y.; Zhu, S.; Li, L. L.; Gu, Z. J.; Zhao, Y. L. Ultrasmall BiOI Quantum Dots with Efficient Renal Clearance for Enhanced Radiotherapy of Cancer. *Adv. Sci.* **2020**, *7*, 1902561.

(8) Giulietti, A. Laser-driven particle acceleration for radiobiology and radiotherapy: where we are and where we are going. *Conference on Medical Applications of Laser-Generated Beams of Particles IV—Review of Progress and Strategies for the Future, Prague, Czech Republic, April*

24−25; SPIE-International Society for Optics and Photonics: Prague, Czech Republic, 2017.

(9) Song, G. S.; Cheng, L.; Chao, Y.; Yang, K.; Liu, Z. Emerging Nanotechnology and Advanced Materials for Cancer Radiation Therapy. *Adv. Mater.* **2017**, *29*, 1700996.

(10) Jiang, W.; Li, Q.; Xiao, L.; Dou, J.; Liu, Y.; Yu, W.; Ma, Y.; Li, X.; You, Y.-Z.; Tong, Z.; Liu, H.; Liang, H.; Lu, L.; Xu, X.; Yao, Y.; Zhang, G.; Wang, Y.; Wang, J. Hierarchical Multiplexing Nanodroplets for Imaging-Guided Cancer Radiotherapy via DNA Damage Enhancement and Concomitant DNA Repair Prevention. *ACS Nano* **2018**, *12*, 5684−5698.

(11) Chen, X.; Song, J.; Chen, X.; Yang, H. X-ray-activated nanosystems for theranostic applications. *Chem. Soc. Rev.* **2019**, *48*, 3073−3101.

(12) Wang, R.; Deng, J.; He, D.; Yang, E.; Yang, W.; Shi, D.; Jiang, Y.; Qiu, Z.; Webster, T. J.; Shen, Y. PEGylated hollow gold nanoparticles for combined X-ray radiation and photothermal therapy in vitro and enhanced CT imaging in vivo. *Nanomedicine* **2019**, *16*, 195−205.

(13) Xia, D.; Hang, D.; Li, Y.; Jiang, W.; Zhu, J.; Ding, Y.; Gu, H.; Hu, Y. Au-Hemoglobin Loaded Platelet Alleviating Tumor Hypoxia and Enhancing the Radiotherapy Effect with Low-Dose X-ray. *ACS Nano* **2020**, *14*, 15654−15668.

(14) Jiang, W.; Li, Q.; Zhu, Z.; Wang, Q.; Dou, J.; Zhao, Y.; Lv, W.; Zhong, F.; Yao, Y.; Zhang, G.; Liu, H.; Wang, Y.; Wang, J. Cancer Chemoradiotherapy Duo: Nano-Enabled Targeting of DNA Lesion Formation and DNA Damage Response. *ACS Appl. Mater. Interfaces* **2018**, *10*, 35734−35744.

(15) De Ruysscher, D.; Niedermann, G.; Burnet, N. G.; Siva, S.; Lee, A. W. M.; Hegi-Johnson, F. Radiotherapy toxicity. *Nat. Rev. Dis. Prim.* **2019**, *5*, 13.

(16) Zhu, D.; Lyu, M.; Huang, Q.; Suo, M.; Liu, Y.; Jiang, W.; Duo, Y.; Fan, K. Stellate Plasmonic Exosomes for Penetrative Targeting Tumor NIR-II Thermo-Radiotherapy. *ACS Appl. Mater. Interfaces* **2020**, *12*, 36928−36937.

(17) Lyu, M.; Zhu, D.; Kong, X.; Yang, Y.; Ding, S.; Zhou, Y.; Quan, H.; Duo, Y.; Bao, Z. Glutathione-Depleting Nanoenzyme and Glucose Oxidase Combination for Hypoxia Modulation and Radiotherapy Enhancement. *Adv. Healthcare Mater.* **2020**, *9*, 1901819.

(18) Liu, Y.; Zhen, W.; Wang, Y.; Song, S.; Zhang, H. Na₂S₂O₈ Nanoparticles Trigger Antitumor Immunotherapy through Reactive Oxygen Species Storm and Surge of Tumor Osmolarity. *J. Am. Chem. Soc.* **2020**, *142*, 21751−21757.

(19) Dong, X.; Cheng, R.; Zhu, S.; Liu, H.; Zhou, R.; Zhang, C.; Chen, K.; Mei, L.; Wang, C.; Su, C.; Liu, X.; Gu, Z.; Zhao, Y. A Heterojunction Structured WO2.9-WSe₂ Nanoradiosensitizer Increases Local Tumor Ablation and Checkpoint Blockade Immunotherapy upon Low Radiation Dose. *ACS Nano* **2020**, *14*, 5400−5416.

(20) Fan, Y.; Tu, W. Z.; Shen, M. W.; Chen, X. M.; Ning, Y. S.; Li, J. J.; Chen, T. F.; Wang, H.; Yin, F. F.; Liu, Y.; Shi, X. Y. Targeted Tumor Hypoxia Dual-Mode CT/MR Imaging and Enhanced Radiation Therapy Using Dendrimer-Based Nanosensitizers. *Adv. Funct. Mater.* **2020**, *30*, 1909285.

(21) Duo, Y. H.; Huang, Y. Y.; Liang, W. Y.; Yuan, R. M.; Li, Y.; Chen, T. F.; Zhang, H. Ultraeffective Cancer Therapy with an Antimonene-Based X-Ray Radiosensitizer. *Adv. Funct. Mater.* **2020**, *30*, 1906010.

(22) Shen, Z.; Liu, T.; Yang, Z.; Zhou, Z. J.; Tang, W.; Fan, W. P.; Liu, Y. J.; Mu, J.; Li, L.; Bregadze, V. I.; Mandal, S. K.; Druzina, A. A.; Wei, Z. N.; Qiu, X. Z.; Wu, A. G.; Chen, X. Y. Small-sized gadolinium oxide based nanoparticles for high-efficiency theranostics of orthotopic glioblastoma. *Biomaterials* **2020**, *235*, 119783.

(23) Sahu, S. P.; Cates, E. L. X-ray Radiocatalytic Activity and Mechanisms of Bismuth Complex Oxides. *J. Phys. Chem. C* **2017**, *121*, 10538−10545.

(24) Yang, S. N.; Yang, Y. L.; Yang, Y.; Zhao, X. Y.; Wang, Q.; Li, B.; Dong, L.; Tian, R.; Bao, Z. R. Iron-Palladium Decorated Carbon Nanotubes Achieve Radiosensitization via Reactive Oxygen Species Burst. *Front. Bioeng. Biotechnol.* **2021**, *9*, 405.

(25) Martin, R. F.; Feinendegen, L. E. The quest to exploit the Auger effect in cancer radiotherapy - a reflective review. *Int. J. Radiat. Biol.* **2016**, *92*, 617−632.

(26) Xie, J. N.; Gong, L. J.; Zhu, S.; Yong, Y.; Gu, Z. J.; Zhao, Y. L. Emerging Strategies of Nanomaterial-Mediated Tumor Radiosensitization. *Adv. Mater.* **2019**, *31*, 1802244.

(27) Chen, H.; Gu, Z.; An, H.; Chen, C.; Chen, J.; Cui, R.; Chen, S.; Chen, W.; Chen, X.; Chen, X.; Chen, Z.; Ding, B.; Dong, Q.; Fan, Q.; Fu, T.; Hou, D.; Jiang, Q.; Ke, H.; Jiang, X.; Liu, G.; Li, S.; Li, T.; Liu, Z.; Nie, G.; Ovais, M.; Pang, D.; Qiu, N.; Shen, Y.; Tian, H.; Wang, C.; Wang, H.; Wang, Z.; Xu, H.; Xu, J.-F.; Yang, X.; Zhu, S.; Zheng, X.; Zhang, X.; Zhao, Y.; Tan, W.; Zhang, X.; Zhao, Y. Precise nanomedicine for intelligent therapy of cancer. *Sci. China: Chem.* **2018**, *61*, 1503−1552.

(28) Hossain, M.; Su, M. Nanoparticle Location and Material-Dependent Dose Enhancement in X-ray Radiation Therapy. *J. Phys. Chem. C* **2012**, *116*, 23047−23052.

(29) Gong, L.; Xie, J.; Zhu, S.; Gu, Z.; Zhao, Y. Application of Multifunctional Nanomaterials in Tumor Radiosensitization. *Acta Phys.-Chim. Sin.* **2018**, *34*, 140−167.

(30) Fan, W.; Tang, W.; Lau, J.; Shen, Z. Y.; Xie, J.; Shi, J. L.; Chen, X. Y. Breaking the Depth Dependence by Nanotechnology-Enhanced X-Ray-Excited Deep Cancer Theranostics. *Adv. Mater.* **2019**, *31*, 1806381.

(31) Wathen, C.; Foje, N.; Avermaete, T.; Miramontes, B.; Chapaman, S.; Sasser, T.; Kannan, R.; Gerstler, S.; Leevy, W. In vivo X-Ray Computed Tomographic Imaging of Soft Tissue with Native, Intravenous, or Oral Contrast. *Sensors* **2013**, *13*, 6957−6980.

(32) Singh, J.; Daftary, A. Iodinated contrast media and their adverse reactions. *J. Nucl. Med. Technol.* **2008**, *36*, 69−74.

(33) Lusic, H.; Grinstaff, M. W. X-ray-Computed Tomography Contrast Agents. *Chem. Rev.* **2013**, *113*, 1641−1666.

(34) Zhang, C.; Ren, J.; Hua, J.; Xia, L.; He, J.; Huo, D.; Hu, Y. Multifunctional Bi₂WO₆ Nanoparticles for CT-Guided Photothermal and Oxygen-free Photodynamic Therapy. *ACS Appl. Mater. Interfaces* **2018**, *10*, 1132−1146.

(35) Feng, L.; Yang, D.; Gai, S.; He, F.; Yang, G.; Yang, P.; Lin, J. Single bismuth tungstate nanosheets for simultaneous chemo-, photothermal, and photodynamic therapies mediated by near-infrared light. *Chem. Eng. J.* **2018**, *351*, 1147−1158.

(36) Zang, Y.; Gong, L.; Mei, L.; Gu, Z.; Wang, Q. Bi₂WO₆ Semiconductor Nanoplates for Tumor Radiosensitization through High-Z Effects and Radiocatalysis. *ACS Appl. Mater. Interfaces* **2019**, *11*, 18942−18952.

(37) Heuer-Jungemann, A.; Feliu, N.; Bakaimi, I.; Hamaly, M.; Alkilany, A.; Chakraborty, I.; Masood, A.; Casula, M. F.; Kostopoulou, A.; Oh, E.; Susumu, K.; Stewart, M. H.; Medintz, I. L.; Stratakis, E.; Parak, W. J.; Kanaras, A. G. The Role of Ligands in the Chemical Synthesis and Applications of Inorganic Nanoparticles. *Chem. Rev.* **2019**, *119*, 4819−4880.

(38) Ren, X.; Huo, M.; Wang, M.; Lin, H.; Zhang, X.; Yin, J.; Chen, Y.; Chen, H. Highly Catalytic Niobium Carbide (MXene) Promotes Hematopoietic Recovery after Radiation by Free Radical Scavenging. *ACS Nano* **2019**, *13*, 6438−6454.

(39) Liu, X.; Xu, Y.; Wu, Z.; Chen, H. Poly(N-vinylpyrrolidone)-Modified Surfaces for Biomedical Applications. *Macromol. Biosci.* **2013**, *13*, 147−154.